Reviews of Electromagnetics, Vol. IV, 2025
EuCAP 2025 Special Issue
DOI: 10.53792/RoE/2025/25009

Reviews of Electromagnetics
EuCAP 2025 Special Issue

Measurement, Modeling and Realization of Mono-static 3D UAV RCS for ISAC Channels

Guangcheng Yu[1], Zhiqiang Yuan[1,2], Wei Fan[1,2]*

Abstract
Realistic unmanned aerial vehicle (UAV) radar cross section (RCS) profiles are essential for integrated sensing and communication (ISAC) channel modeling, ensuring reliable prediction and evaluation of sensing performance. Despite advancements in UAV RCS research, the limited experimental data and the unestablished realistic UAV RCS model, particularly for 3D scenarios, have resulted in the unavailability of practical UAV RCS profiles. This study focuses on modeling and realizing UAV RCS based on an 3D UAC RCS measurement. First, we conduct mono-static 3D UAV RCS measurements in an anechoic chamber, covering a frequency band of 1.8 GHz to 18.2 GHz and azimuth angles of -90° to 90° (given the symmetry of the UAV) at three UAV elevation angles $\{0^\circ, 90^\circ, 180^\circ\}$. Next, the measured RCS data are fitted to three well-known distributions: Rician, Gamma, and LogNormal. The analysis indicates that the Rician distribution is recommended for modeling UAV RCS based on the fitting performance. Detailed distribution parameters are provided for UAV RCS realization. Furthermore, a statistical evaluation of the UAV RCS based on the modeling results is performed, providing insights for UAV sensing prediction and assessment. Finally, the validated model is utilized to generate UAV RCS data, which exhibits a strong agreement with measured results. These findings facilitate the advancement of ISAC channel research and practical applications.

Key terms
UAV; ISAC channel modeling; Mono-static measurement; RCS modeling and realization.

[1] *National Mobile Communications Research Laboratory, School of Information Science and Engineering, Southeast University, Nanjing, China*
[2] *Purple Mountain Laboratories, Nanjing, China*
***Corresponding author**: weifan@seu.edu.cn

Received: 22/05/2025, Accepted: 01/08/2025, Published: 28/11/2025

1. Introduction

Integrated sensing and communication (ISAC) is emerging as a cornerstone for the advancement of 6G networks, facilitating improvements in system ubiquity and connectivity [1]. By integrating hardware and software components, ISAC exhibits substantial potential to support various industrial applications [2], particularly aerial networks, autonomous driving, advanced driver-assistance systems [3].

To design, develop and assess the ISAC systems, an accurate yet realistic channel model is essential [4], [5]. However, the sensing part of ISAC involves diverse point-to-multipoint scenarios that are not adequately captured by existing communication-focused channel models [6], e,g., 3GPP TR 38.901 [7]. A fundamental difference between sensing and communication lies in the presence of backscattering from multiple targets, quantified by the radar cross section (RCS), which characterizes the scattering-induced signal loss [8]. Furthermore, traditional sensing systems (e.g., radar) primarily characterize the instantaneous properties of radio channels, while current ISAC systems require knowledge of the statistical behavior of sensing targets to meet specific detection probability and false alarm rate requirements [9]. In addition, the mono-static behavior of sensing targets introduces self-interference, posing challenges for configuring full-duplex ISAC systems [10]. Therefore, developing statistical RCS models for typical objects is critical to closing the gap in ISAC channel studies.

RCS modeling has garnered significant interest from both standardization and industry [3], [6], [10]. Recent studies, such as [12] and [13], have focused on RCS measurements of typical road objects, such as bicycles, automobiles, and motorcycles. With unmanned aerial vehicles (UAVs) envisioned as key components in future 6G systems, accurate RCS measurement, modeling and realization for such objects has become essential [14]. For instance, [15] the analyzed the RCS of multirotor UAV through simulation, though no empirical validation was provided. Subsequently, [16] conducted the UAV RCS measurement in a laboratory environment with radar-absorbing materials, revealing the random distribution pattern of RCS values with observation angles. Furthermore, [10] conducted the UAV RCS measurement in an anechoic chamber, and proposed an omnidirectional model (i.e., RCS values are assumed constant across all angles) for the UAV RCS.

Despite these advancements, significant gaps still remain in current UAV RCS studies: 1) the lack of experimental data on UAV RCS, particularly for 3D scenario; 2) the absence of realistic model that accurately captures the RCS fading distribution with respect to angle and frequency; and 3) the unavailability of statistical analysis and recommendations for UAV RCS modeling and realization. Note that our previous work [11] have conducted the measurement and modeling of UAV RCS. Building upon this foundation, this work further conducts an in-depth experimental analysis of UAV RCS for developing comprehensive and realistic UAV RCS model, and exploits the well-established model for realizing future UAV RCS. In summary, this work conducts the measurement, modeling and realization on UAV RCS, with the following key contributions.

- A monostatic 3D UAV RCS measurement is introduced in an anechoic chamber, covering azimuth angles from –90° to 90° and frequencies ranging from 1.8 GHz to 18.2 GHz at three UAV elevation angles $\{0°, 90°, 180°\}$.
- A recommendation model is proposed. The measured RCS values are fitted across all azimuth angles at each frequency and elevation angle for modeling. After evaluation, the Rician distribution is recommended for UAV RCS modeling, and the corresponding distribution parameters are provided.
- Analysis of the modeling results indicates that 1) under poor sensing conditions (i.e., without dominant scattered components), the (normalized) UAV RCS power falls below -20 dBsm and -10 dBsm with probabilities of 1% and 10% respectively; and 2) under favorable conditions (i.e., with dominant components), the corresponding RCS thresholds increase to -18.5 dBsm and -8.5 dBsm.
- The proposed model is realized for practical implementation and its performance is evaluated. Analysis of the model-generated results indicates that the model-generated UAV RCS closely matches the measured UAV RCS, with an root mean square error (RMSE) below 0.051 in the cumulative distribution function (CDF) and maximum errors under 0.75 dBsm and 0.05 in mean and standard deviation.

2. UAV RCS Measurement

2.1. Measurement setup

As shown in Fig. 1, we conducted the mono-static 3D UAV RCS measurement in an anechoic chamber. Here, the device under test (DUT), i.e., sensing target, was a DJI Phantom 3 UAV, which features four symmetrical rotors, a horizontal diagonal of 35 cm, and a height of 20 cm. The UAV was placed at the center of a turntable, enabling the measurement of its response at different azimuth angles through rotation.The rotation range was from -90° to 90° (given the symmetry of UAV) in the step of 2°, i.e., $\phi = [-90° : 2° : 90°]$. Three UAV elevation sides including the top, azimuth plane, and bottom, were considered in the measurements, i.e, $\theta = \{0°, 90°, 180°\}$. Both the transmitter (TX) and receiver (RX) were equipped with vertically polarized directional antennas. Although a finer step size might be required at higher frequencies, and RCS should ideally be measured across all polarization states, this configuration was chosen due to the limited measurement time.

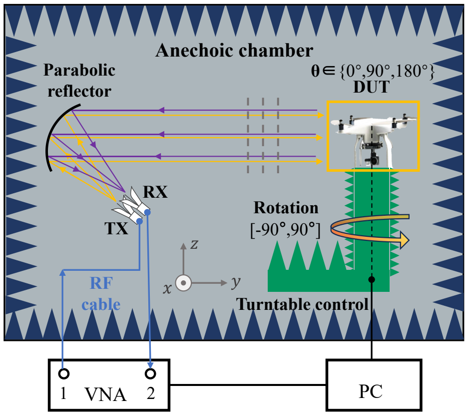

Figure 1: Illustration of the mono-static 3D UAV RCS measurement.

The compact antenna test range (CATR) scheme was used to access the far-field RCS of UAV [17]. A two-port vector network analyzer (VNA) was used to collect the channel frequency response (CFR), i.e., $S_{21}(f)$. The frequency was swept from 1.8 GHz to 18.2 GHz, with 2801 frequency points at each azimuth angle, resulting in an ambiguity bound of 170.7 ns and a delay resolution of 0.06 ns. The effect of the UAV's rotating propeller blades on the observed RCS, refereed to as the Micro-Doppler effect [9], was not considered in this study, as measuring the influence of the rapidly moving blades was not feasible due to the long sweep duration of the VNA. This effect will be appropriately modeled in future work, given its significance.

2.2. Measurement procedure

To obtain accurate RCS results, it is essential to eliminate the effects of undesired reflections from the background and parasitic scatters that are not associated with the target. Furthermore, since the received power is proportional to the RCS of the target, the absolute RCS can be determined by comparing the measured received power with that of a known calibration object, such as a perfect electrically conducting sphere with a known RCS [13]. Accordingly, the measurement campaign involves measuring the background, calibration sphere, and DUT.

The measurement procedure consists of three stages: *i) Background measurement*: Collect the CFR of the background without the DUT on the turntable, as $S_{21}^{\mathrm{BG}}(f)$; *ii) Calibration sphere measurement*: Place a metallic sphere of 17.8 cm radius (RCS as σ^{Cal} = -10 dBsm) at the center of the turntable, and collect its CFR $S_{21}^{\mathrm{Cal}}(f)$; and *iii) DUT measurement*: Place the UAV at the center of the turntable, and collect the CFR for each rotational angle at each frequency point, as $S_{21}^{\mathrm{Cal}}(f)$.

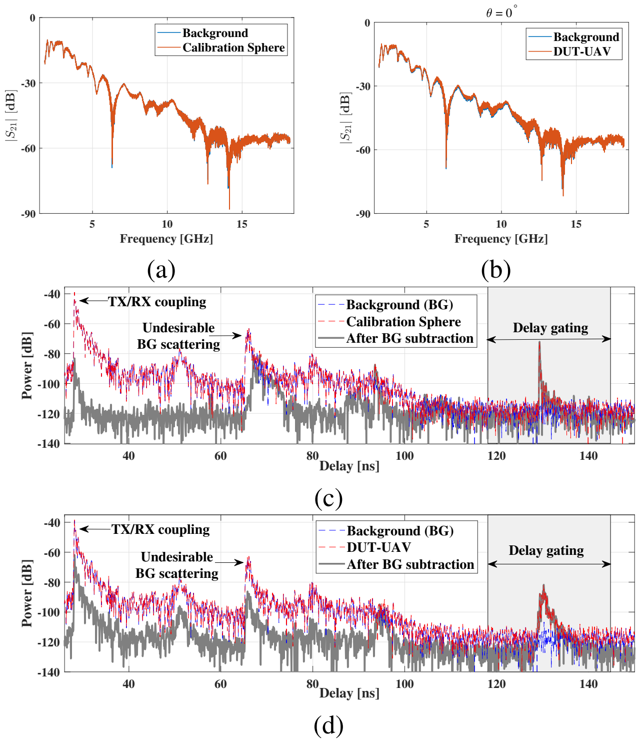

(a) (b)

(c)

(d)

Figure 2: Intermediate RCS data processing results: measured CFRs (i.e., $|S_{21}|$) for calibration sphere (a) and UAV (b) with referring background response, and CIRs for calibration sphere (c) and UAV (d) before and after background subtraction.

2.3. Data processing

The overall procedure for processing raw data to obtain the absolute target RCS is outlined as follows:

1) Background Subtraction: This step aims to mitigate the influence of undesired background scatterings. It is achieved by subtracting the background CFR $S_{21}^{\text{BG}}(f)$ from the collected CFRs of both the calibration sphere $S_{21}^{\text{Cal}}(f)$ and the UAV $S_{21}^{\text{Cal}}(f)$ under phase-coherent conditions. Mathematically, the post-background subtraction CFRs of the calibration sphere and the DUT, denoted as $S_{21,\text{bs}}^{\text{Cal}}(f)$ and $S_{21,\text{bs}}^{\text{DUT}}(f)$, can be given by

$$\begin{aligned} S_{21,\text{bs}}^{\text{Cal}}(f) &= S_{21}^{\text{Cal}}(f) - S_{21}^{\text{BG}}(f) \\ S_{21,\text{bs}}^{\text{DUT}}(f,\phi) &= S_{21}^{\text{DUT}}(f,\phi) - S_{21}^{\text{BG}}(f) \end{aligned} \tag{1}$$

2) Delay gating: This step aims to isolate the target scattering from reflections within the measurement range. It is achieved by adding a delay gate, which is determined based on the propagation distance and compared with the background response. Specifically, first, the CFRs obtained after background subtraction are converted into channel impulse responses (CIRs) via an inverse Fourier transform, commonly referred to as range profiles; next, a 6th-order Kaiser window function, with a predefined delay range, is applied to the CIRs; finally, the gated CIRs are transformed back into the frequency domain. The resulting CFRs of the calibration sphere and UAV are denoted as $S_{21,\text{bs,g}}^{\text{Cal}}(f)$ and $S_{21,\text{bs,g}}^{\text{DUT}}(f,\phi)$, respectively.

3) RCS calibration: This step aims to express the absolute UAV RCS in absolute numerical values. Mathematically, the absolute UAV RCS can be derived as the ratio of the received power from the DUT to that from the reference sphere, with the reference sphere RCS serving as the calibration standard. This relationship is expressed as:

$$\sigma^{\text{DUT}}(f,\phi) = \left|S_{21,\text{bs, g}}^{\text{DUT}}(f,\phi)\right|^2 \Big/ \left|S_{21,\text{bs, g}}^{\text{Cal}}(f)\right|^2 \cdot \sigma^{\text{Cal}}. \tag{2}$$

3. Experimental results

Fig. 2 shows the intermediate results from the data processing. From Fig. 2(a) and Fig. 2(b), it is evident that the background response significantly overwhelms the target response, which highlights the crucial role of background subtraction in the data processing. Fig. 2(c) and Fig. 2(d) show the CIRs of the sphere and the UAV, respectively, before and after the background subtraction, where the TX/RX coupling effects and undesirable background scattering are effectively removed. Next, a delay gating is added to isolate the scattered components from the target objects to obtain the RCS.

Fig. 3 shows the range-azimuth profiles (top), photos (middle) and RCS (bottom) of the UAV for different elevation angles. Here, the radar image undergoes delay gating and spatial inversion from the outer edge to the center of the turntable, to explicitly present the outside contour of the UAV. From Fig. 3(middle), the pink, red, and blue semicircular markers indicate the UAV's horizontal length (28.95 cm), diagonal span (35 cm), and horizontal width (28.9 cm), respectively. Fig. 3(top) presents a drone-like pattern. Here, the range response difference between the blades (longer range) and the UAV body (shorter range) is evident. From Fig. 3(bottom), it is observed that 1) the overall RCS values span from -40 dBsm to 5 dBsm; 2) the averaged RCS values at $\theta = 90^\circ$ are slightly higher than that at $\theta = 0^\circ$ and $\theta = 180^\circ$; and 3) rapid fluctuation in both frequency and angle domains, resulting from the constructive and destructive superposition of scattered field components (i.e., small-scale fading).

Fig. 4 presents the variation of the UAV RCS with azimuth angles at three specific frequencies. It is evident that the RCS fluctuates with the angles, and the extend of these fluctuations increases with frequency. This can be explained by 1) the presence of thin objects (e.g., blades) ; and 2) the growing electrical size of the DUT with increasing frequency (i.e., the spatial span in wavelengths expands, thereby reducing angular coherence). Note that the angular step resolution in RCS measurements may be insufficient for detailed target interpretation. However, given that this work focuses on statistical RCS analysis, the angular resolution does not represent a significant limitation. Furthermore, the angle-averaged RCS values exhibit an increasing trend with frequency (also shown in Fig. 6(top)). Therefore, exploiting statistical models to capture the RCS distributions across angles at each frequency is a reasonable approach.

4. UAV RCS Modeling

This section aims to develop a statistical model for UAV RCS, offering valuable insights and frameworks for future RCS realization, prediction, and assessment. Traditionally, radar detection performance is characterized by assuming that RCS follows

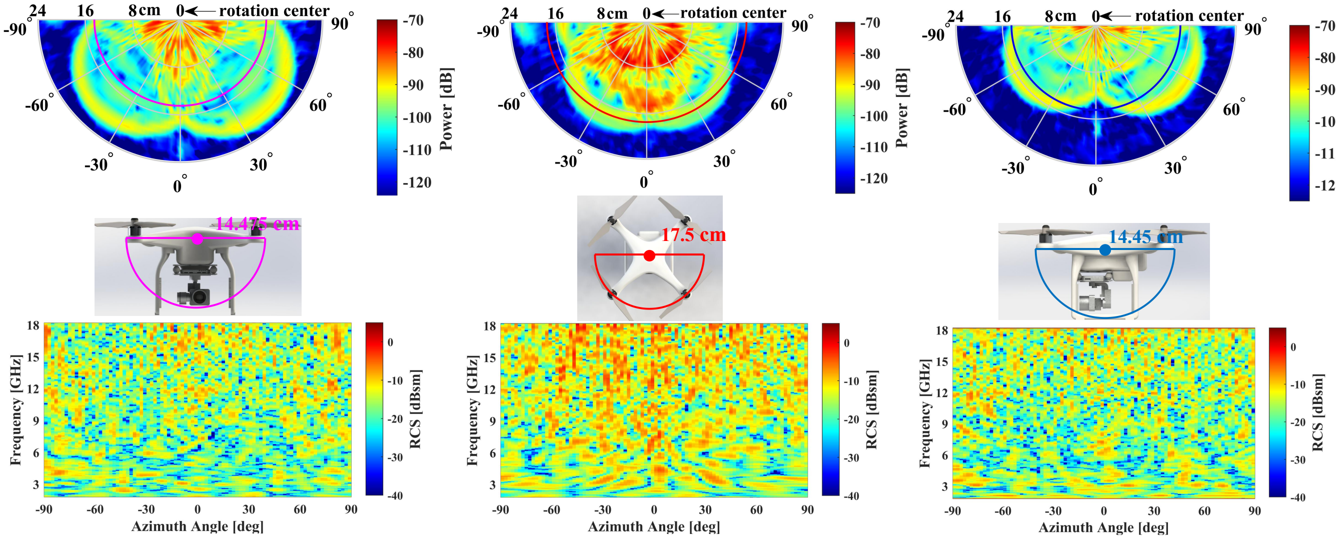

(a) (b) (c)

Figure 3: Range-azimuth profiles (top), photos (middle) and RCS values (bottom) of the UAV for different elevation angles,including: (a) $\theta = 0°$, (b) $\theta = 90°$, and (c) $\theta = 180°$.

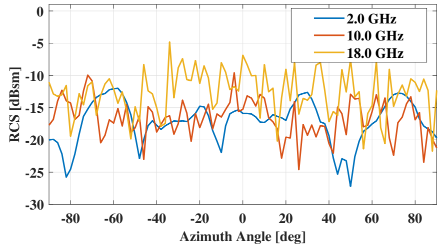

Figure 4: UAV RCS versus the azimuth angle at three specific frequencies.

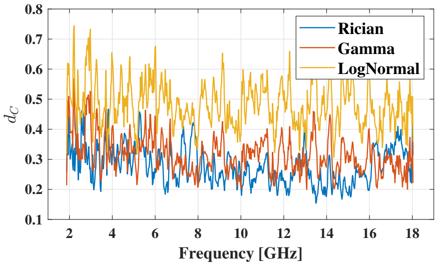

Figure 5: Average CVM distance d_c across the elevation domain ($\theta = \{0°, 90°, 180°\}$) for the three fittings.

one of the Swerling distributions I-IV [18]. However, practical applications have revealed limitations of these models [19], as RCS fluctuations for certain targets cannot consistently conform to these distributions. One such example is highlighted in this paper, where the Rayleigh distribution (Swerling III/IV) fails to adequately model the UAV RCS, as shown in Fig. 7. Hence, three widely recognized distributions,i.e., Rician, Gamma, and LogNormal, are introduced to characterize the signal field superposition and fit the measured RCS values. Importantly, the introduced distributions encompass all four Swerling models, as the exponential and Rayleigh distributions (the foundational distributions for Swerling I-IV) are special cases of the Gamma and Rician distributions.

The fitting process with the measured data is conducted by considering the RCS values across different azimuth angles with the frequency given. The parameters of the distributions used in the fitting are estimated using maximum likelihood estimation, incorporating the cumulative distribution functions (CDFs) of the fitted distributions along with the empirical data. To evaluate the fitting performance, the Cramer–Von Mises (CVM) distance metric is introduced [18], defined as:

$$d_C(f) = \sqrt{\frac{1}{12M} + \sum_{i=1}^{M} \left| F_\chi \left(\sigma^{\text{DUT}} \, (f, \phi_j) \right) - \frac{2j-1}{2M} \right|^2}, \quad (3)$$

where M is the number of rational angles, $\mathscr{F}_\chi(x)$ is the distribution CDF with the estimated parameter χ. The optimal model can be chosen based on the minimum CVM value.

Fig. 5 shows the CVM values for different fittings. It is evident that the Rician distribution yields the most favorable fitting results, attaining the lowest CVM values in the majority of frequency cases. The average CVM distances for the Rician, Gamma, and LogNormal distributions are 0.28, 0.31, and 0.48, respectively. These results suggest that the Rician distribution effectively captures the superposition of multiple scattered field components on the UAV. Therefore, it is recommended to use the Rician distribution for the statistical model of UAV RCS.

Fig. 6 shows the Rician fitting results, with the distribution parameters detailed for each frequency. From Fig. 6(top), it is evident that 1) the measured RCSs matches well with the Rician-fitted results in both the mean and standard deviation, for all frequencies and elevation angles, indicating that the Rician distribution, with the estimated parameters, can accurately model the UAV RCS; and 2) a upward trend in the mean RCS with increasing frequency, suggesting that the UAV becomes electrically larger as frequency increases. Furthermore, a linear regression analysis is performed on the mean and standard deviation values

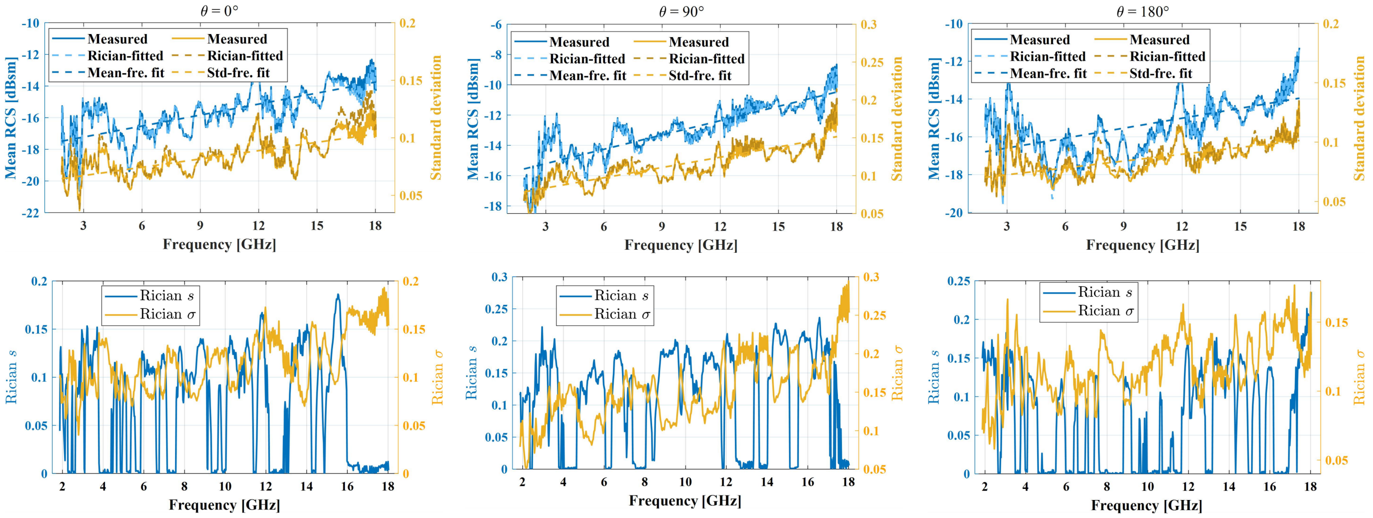

(a) (b) (c)

Figure 6: Rician fitting results, including the mean and deviation of the measured and Rician-fitted RCS (top) and the distribution parameters (bottom).

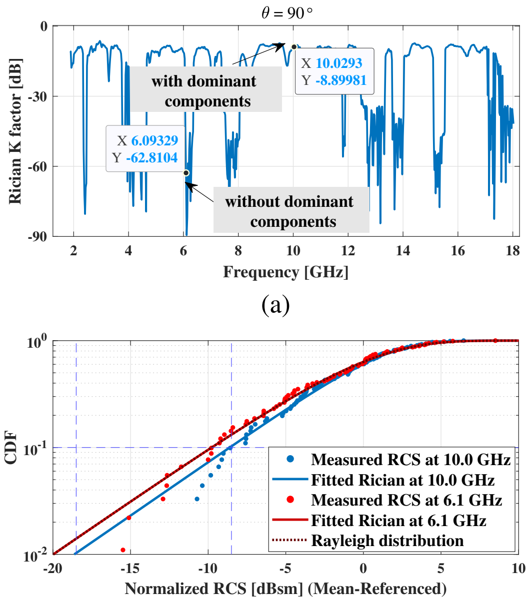

(b)

Figure 7: (a) The K factor of the Rician fittings and (b) CDFs of the normalized RCS power at 10.0 GHz and 6.1 GHz for $\theta = 90°$. Note that in (b) the Rayleigh distribution overlaps with the Rician fitting at 6.1 GHz (due to the large K).

for the frequency. Here, the mean fitting is modeled as $\mu = a \cdot f + b$, and variance fitting as $\varepsilon = c \cdot f + d$, respectively, where $\{a, b, c, d\}$ are the regression parameters. These parameters are calculated as: for $\theta = 0°$, $\{0.231, -17.92, 0.0024, 0.06\}$; for $\theta = 90°$, $\{0.315, -16.15, 0.0045, 0.07\}$; and for $\theta = 180°$, $\{0.175, -17.12, 0.0019, 0.07\}$. Despite some deviations, it is evident that a good match between the measured data and the fitted linear function. Fig. 6 (bottom) details the Rician fitting parameters. These empirical results provide essential input parameters for RCS modeling and realization, thereby improving the predictive accuracy of UAV RCS for future ISAC systems.

To further reveal the RCS characteristics, Fig. 7(a) presents the K factors of the Rician fittings with $\theta = 90°$. It is evident that the K factors fluctuate around -10 dB at some frequencies, while significantly smaller (e.g., below -30 dB) at other frequencies. These results indicate the presence or absence of dominant field components at different frequencies, resulting from the wavelength-dependent scattering behavior (as mentioned before) of the UAV surface. Two Rician fitting examples, i.e., one at 10.0 GHz with a large K-factor of -8.9 dB, and another at 6.1 GHz with a small K-factor of -62.8 dB, are chosen for demonstration, as highlighted in Fig. 7(a). The measured RCS and the fitting results for these two frequencies are further shown in Fig. 7(b). It is evident that the discrepancies between the measured data and the fitted curve in the low-K scenario may be due to limited data availability. However, this has minimal effect on the overall analysis, as the associated probability density is very low, i.e, 10^{-2}. Furthermore, under favorable conditions (i.e., with dominant components), the normalized RCS power falls below -8.5 dBsm and -18.5 dBsm with probabilities of 10% and 1 %, respectively. In contrast, under poor sensing conditions (i.e., without dominant components), the corresponding power thresholds shift to -10 dBsm and -20 dBsm. These characteristics offer valuable guidance for UAV RCS modeling in future ISAC studies.

5. UAV RCS Realization

To realize, predict and assess the future UAV RCS, this section utilizes the developed statistical model for UAV RCS to generate corresponding values, which are subsequently compared with the experimentally measured RCS data.

Fig. 8 compares the CDFs of model-generated and measured RCS power at 5.0 GHz for three elevation angles. It is evident that the CDF of model-generated RCS power closely matches that of the measured RCS power, with the RMSEs for $\theta = \{0°, 90°, 180°\}$ being $\{0.036, 0.023, 0.051\}$. These re-

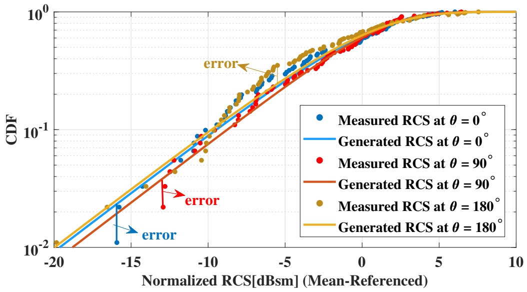

Figure 8: CDFs of model-generated and measured RCS power at 5.0 GHz for three elevation angles.

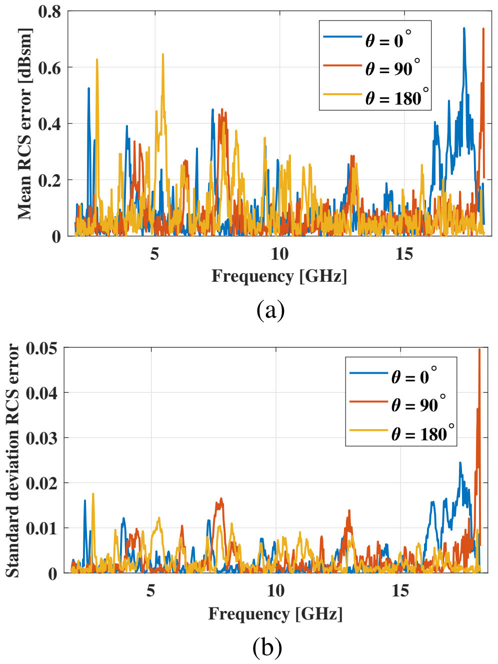

(a)

(b)

Figure 9: Comparison between model-generated and measured RCS at three elevation angles: (a) mean RCS error; (b) standard deviation RCS error.

sults indicate that the developed statistical model can effectively generate UAV RCS.

To further assess the performance of the model-generated results, Fig. 9 compares the model-generated and measured RCS in terms of both mean error (i.e., Fig. 9(a)) and standard deviation error (i.e., Fig. 9(b)) at three elevation angles. It is evident that the model-generated RCS aligns well with the measured RCS. The maximum mean errors for $\theta = \{0°, 90°, 180°\}$ are $\{0.74, 0.74, 0.65\}$ dBsm, and the maximum standard deviation RCS errors for $\theta = \{0°, 90°, 180°\}$ are $\{0.02, 0.02, 0.05\}$. These results suggest that the proposed statistical model offers a reliable framework for generating UAV RCS, providing valuable insights for future ISAC research.

6. Conclusion And Future Work

This letter focuses on the measurement, modeling and realization of the 3D UAV RCS. First, the measurements were conducted covering azimuth angles of –90° to 90° and frequencies of 1.8 GHz to 18.2 GHz for three UAV elevation angles $\{0°, 90°, 180°\}$. To ensure accurate RCS data acquisition, background and metallic sphere responses were recorded for background subtraction and calibration, respectively. The measured RCS spans from –40 dBsm to 5 dBsm and fluctuates with angles due to constructive and destructive superposition of scattered components. The range-azimuth profiles exhibit a drone-like pattern, with the blades showing longer range responses than the body. Next, the acquired RCS data were fitted to Rician, Gamma, and Log-Normal distributions, with the Rician model recommended for its superior fitting performance. The frequency-dependent variation of the Rician K-factor reveals the role of dominant scatterers influenced by wavelength. Under poor-sensing conditions, the probabilities of normalized RCS power falling below -20 dBsm and -10 dBsm are 1% and 10%, respectively, while these thresholds shift to -18.5 dBsm and -8.5 dBsm under more favorable conditions.

The developed statistical model is further exploited to generate UAV RCS, achieving an RMSE below 0.051 in the CDF and maximum errors under 0.75 dBsm and 0.05 in mean and standard deviation. Importantly, the successful realization of statistical RCS generation process is crucial for practical deployment in ISAC systems. This realization bridges the gap between theoretical formulation and system-level application, enabling real-time synthesis of realistic RCS profiles essential for sensing-aided communication and joint waveform design. In dynamic and complex electromagnetic environments, such capability ensures sensing components can reliably detect and characterize targets while maintaining seamless coordination with communication functionalities.

A thorough investigation of RCS is essential for ISAC channel modeling, awaiting future research. In our future work, we will: 1) introduce additional UAV RCS models, covering diverse physical characteristics (e.g., size) and materials, while incorporating more elevation sensing angles and micro-Doppler effects [9], based on a broad set of experimental data; 2) explore the extrapolation of the proposed model to more practical bi-static and multi-static configurations; 3) expand our study to include a variety of representative objects, such as motorcycles, cars, traffic signs, and humans, focusing on RCS measurement, modeling and realization in mono-static, bi-static, and multi-static configurations; and 4) examine the RCS characteristics and frequency dependencies across FR1, FR2, and FR3. Emphasize that these extensive measurements will require collaborative efforts from both industry and standardization bodies, and this work represents the initial step towards achieving that goal.

Acknowledgment

This work was supported by the start-up Research Fund of Southeast University, China, under Grant RF1028623309, by Beijing Natural Science Foundation under Grant L243002, by the China Postdoctoral Science Foundation under Grant Number 2024M760433, and by the Open Project of Key Laboratory of the Fifth Institute of Electronics, Ministry of Industry and Information Technology under Grant Number IPQERT(KL)-2024-02.

References

[1] "Framework and overall objectives of the future development of IMT for 2030 and beyond", ITU, Geneva, Switzerland, Tech. Rep. ITU-RM.2160, 2023.

[2] R. Thomä, T. Dallmann, S. Jovanoska, P. Knott and A. Schmeink, "Joint communication and radar sensing: An overview", *in 2021 15th European Conference on Antennas and Propagation*, pp. 1–5, 2021.

[3] "Information on ISAC channel modeling", 3GPP, Sophia Antipolis Cedex, France, Tech. Rep. TSG RAN WG1 #116bis R1-2403107, Apr. 2024. [Online]. Available: https://www.3gpp.org/ftp/tsg_ran/WG1_RL1/TSGR1_116b/Docs/R1-2403107.zip.

[4] Y. Liu, J. Zhang, Y. Zhang, Z. Yuan and G. Liu, "A shared cluster-based stochastic channel model for integrated sensing and communication systems", *IEEE Transactions on Vehicle Technology*, Vol. 73, no. 5, pp. 6032–6044, 2024.

[5] Z. Yuan, G. Yu, Y. Lyu, J. Zhang, F. Zhang and W. Fan, "Site-Specific Ray-Tracing and Experimental Validation for THz Channel Characterization", *IEEE Transactions on Terahertz Science and Technology*, Vol. 15, no. 3, pp. 319–331, 2025.

[6] Keysight, "6G FR3 channel emulation and ISAC", Application notes, 2024. [Online]. Available: https://www.keysight.com/us/en/assets/3124-1310/application-notes/6G-FR3-Channel-Emulation-and-ISAC.pdf

[7] "Study on channel model for frequencies from 0.5 to 100 GHz", 3GPP, Sophia Antipolis Cedex, France, Tech. Rep. TR 38.901 V14.0.0, Mar. 2017.

[8] Z. Yuan, L. Yu, Z. Wang, C. Li, T. Dallmann and W. Fan, "Experimental Analysis and Modeling of Monostatic AAV RCS for ISAC Channels", *IEEE Antennas and Wireless Propagation Letters*, Vol. 24, no. 1, pp. 222–226, 2025.

[9] H. C. A. Costa, S. J. Myint, C. Andrich, S. W. Giehl, C. Schneider and R. S. Thomä, "Modeling micro-Doppler signature of drone propellers in distributed ISAC", *in 2024 IEEE Radar Conference*, pp. 1–6, 2024.

[10] "Channel modelling for ISAC", 3GPP, Sophia Antipolis Cedex, France, Tech. Rep. TSG-RAN WG1 Meeting #117 R1-2403921, May 2024. [Online]. Available: https://www.3gpp.org/ftp/tsg_ran/WG1_RLI/TSGR1_117/Docs/R1-2403921.zip.

[11] Z. Yuan, L. Yu, C. Li and W. Fan, "On Experimental Analysis of Mono-Static 3D UAV RCS for ISAC Channel Modeling", *in 2025 19th European Conference on Antennas and Propagation* , pp. 1–5, 2025.

[12] A. Schwind, W. Hofmann, R. Stephan and M. A. Hein, "Bi-static RCS variations of pedal and wheel movements on bicycles between 1 and 10 GHz", *in 2021 Antenna Measurement Techniques Association Symposium*, pp. 1–6, 2021.

[13] S. B. J. Gowdu, A. Schwind, R. Stephan and M. A. Hein, "Monostatic RCS measurements of representative road traffic objects in the 76...81 ghz frequency band", *in 2020 IEEE Radar Conference*, pp. 1–6, 2020.

[14] F. Liu, L. Zheng, Y. Cui, C. Masouros, A. P. Petropulu and H. Griffiths, "Seventy years of radar and communications: The road from separation to integration", *IEEE Signal Processing Magazine*, Vol. 40, no. 5, pp. 106–121, 2023.

[15] Z. Xie, H. Zhou, Y. Zou and C. Liu, "RCS simulation of small multi-rotor unmanned aerial vehicle", *in 2022 International Applied Computational Electromagnetics Society Symposium*, pp. 1–4, 2022.

[16] M. Rosamilia, A. Aubry, A. Balleri, V. Carotenuto and A. De Maio, "RCS simulation of small multi-rotor unmanned aerial vehicle", *in 2022 IEEE 9th International Workshop on Metrology for AeroSpace*, pp. 179–184, 2022.

[17] L. M. Tancioni, A. Jernberg, P. Noren, A. Giacomini, A. Scannavini and L. Foged, "Over-the-air testing of active antenna system base stations in compact antenna test range", *in 2019 13th European Conference on Antennas and Propagation*, pp. 1–5, 2019.

[18] P. Swerling, "Radar probability of detection for some additional fluctuating target cases", *IEEE Transactions on aerospace and electronic systems*, Vol. 33, no. 2, pp. 698–709, 1997.

[19] A. De Maio, A. Farina and G. Foglia, "Target fluctuation models and their application to radar performance prediction", *IEEE Proceedings-Radar, Sonar and Navigation*, Vol. 151, no. 5, pp. 261–269, 2004.

[20] K. E. Baddour and T. J. Willink, "Improved estimation of the Ricean K factor from I/Q fading channel samples", *IEEE Transactions on Wireless Communications*, Vol. 7, no. 12, pp. 5051–5057, 2008.